Ultrasonic imaging of buried defects in rails

Samuel Rodriguez, Victor Gayoux, Eric Ducasse, Michel Castaings, Nicolas Patteeuw

Ultrasonic imaging of buried defects in rails

Samuel Rodriguez [a,*], Victor Gayoux [a], Eric Ducasse [b], Michel Castaings [c], Nicolas Patteeuw [d]

[a] University of Bordeaux, CNRS, Arts et Metiers Institute of Technology, Bordeaux INP, INRAE, I2M Bordeaux, F-33400 Talence, France
[b] Arts et Metiers Institute of Technology, University of Bordeaux, CNRS, Bordeaux INP, INRAE, I2M Bordeaux, F-33400 Talence, France
[c] Bordeaux INP, University of Bordeaux, CNRS, Arts et Metiers Institute of Technology, INRAE, I2M Bordeaux, F-33400 Talence, France
[d] SNCF Réseau, Direction générale industrielle et ingénierie, 9 quai de Seine, 93584 Saint-Ouen Cedex, France

Nondestructive testing
Ultrasonic waves
Rail
Topological imaging
Reverberation

ABSTRACT

The present work addresses the ultrasonic NDT of rails, more precisely of the rail foot. The practical constraint is that transducers must be located on the rail head, whereas the region of interest is the rail foot. Thus, there is no direct acoustic path between the transducers and the region of interest. As classical delay and sum methods cannot be applied to such cases, the goal of the paper is to numerically assess the potentiality of the topological imaging method to investigate the rail foot. Three specific typical rail foot defects are investigated, namely, longitudinal vertical cracks, corrosion pits and rail injuries. Simulating eight transducers with different polarizations, the images obtained show that the detection and approximate location of the various defects are possible.

1. Introduction

Rails are subject to high transient mechanical loads. Internal cracks or impact damages can be found in the rail head, web and foot. Loss of material due to corrosion may also appear in the web and foot, especially in humid environments such as tunnels. Early flaw detection is thus required to avoid railway failures that may lead to tragic accidents. The rail network inspection can be made locally or with rail testing trains to cover wide network parts. Different NDT methods are used based on electromagnetism, eddy currents, or ultrasound [1]. Many methods aim at detecting near-surface or in-head flaws using either surface waves [2] or bulk waves [3]. Using rail-guided waves allows the inspection of the whole rail section from a distance [4]. Some devices are especially designed to inspect the rail foot. Hu et al. [5] performed local measurements with transducers directly located on the foot generating locally guided waves. Pathak et al. [6] used contactless transducers to assess the possibility of a rail foot-monitoring moving device. Despite the interest of these methods [5,6], they are limited to defect detection, and no in-rail section location has been performed.

The purpose of the present work is to numerically study the capability of topological imaging [7–9] to detect and locate defects buried in the rail foot with transducers located on the rail head using the reverberated field. The topological imaging principle was experimentally validated in [9] for the case of a half-cut metal plate and a single transducer in the absence of a direct wave path between the transducer and the region of interest, thus mimicking a buried defect. Taking advantage of the full reverberated acoustic field, sufficient information was measured and successfully used to accurately detect, locate and build images of defects. The success of this study constitutes a solid basis for the rail case, as there is also no direct wave path between the transducer(s) located on the rail head and the rail base, which is the region to be interrogated. However, the method described in [9] cannot be applied as such to practical NDT cases because measuring the whole reverberating field is time consuming and essentially because this reverberated acoustic response is very sensitive to any change in the medium, not only to defects. For instance, a slight shift in the boundary conditions or in the mechanical properties may have significant effects on the acoustic reverberated field and thus on the detection and imaging of sought defects. The solution chosen here to overcome this issue is to truncate the reverberated acoustic field above a chosen time so that it contains sufficient acoustic information on the region of interest without making the method too sensitive to other variations. Typically, for the rail case, the duration should be chosen long enough so that acoustic waves generated by the transducer(s) located on the rail head reach the foot edges and propagate back to the transducer(s) once or twice. In this study, the propagation along the rail axis is neglected so that the inspection is performed in a rail section. Thus, the synthetic measurements and the imaging process are performed over a rail section.

The numerical model and its experimental validation are first presented. Then, the investigated defects and the imaging procedure are

https://doi.org/10.1016/j.ndteint.2022.102737

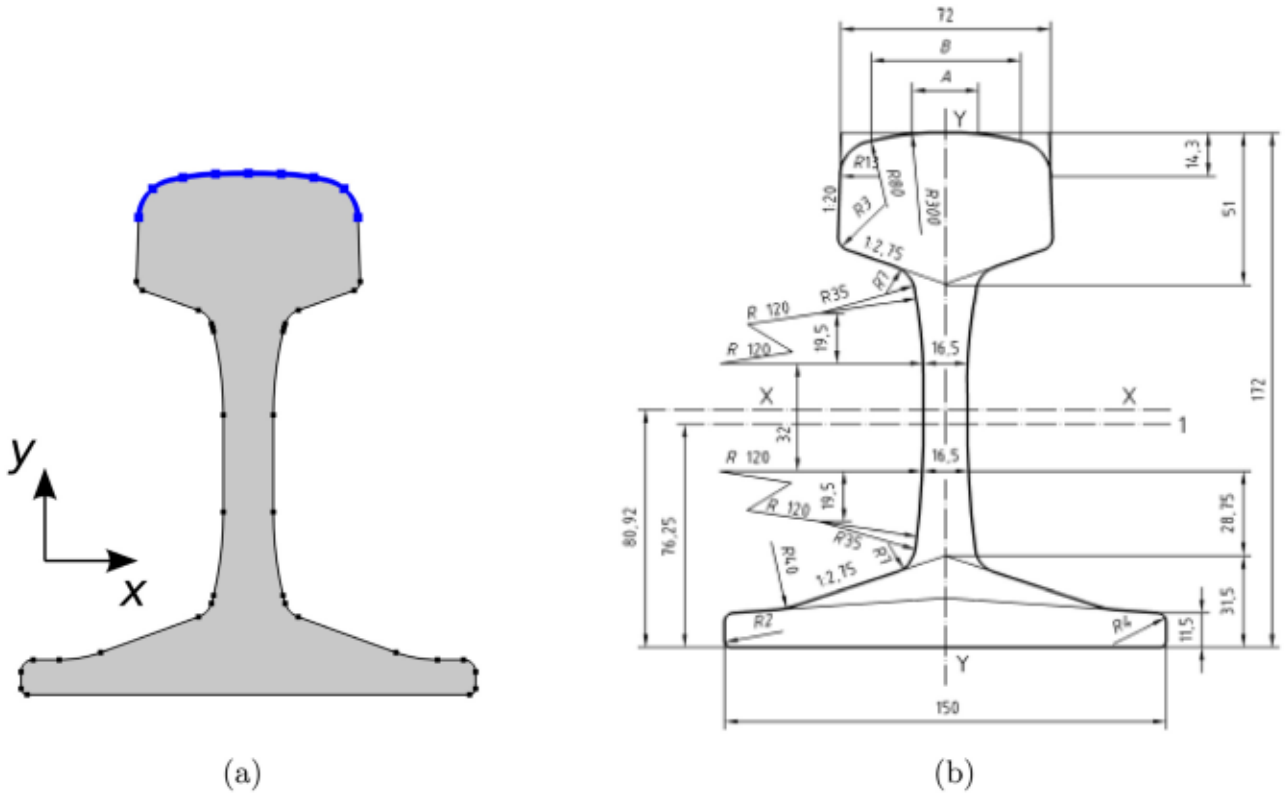

Fig. 1. (a) Model geometry and transducer array location in thick blue. The array is composed of 8 emitter–receivers. (b) Dimensions of the rail profile 60E1 used in the simulations. (For interpretation of the references to color in this figure legend, the reader is referred to the web version of this article.)

Table 1
Experimental stiffness coefficients of the rail steel sample.

Coefficient	Value [GPa]	Accuracy [%]	
		Real part	Imaginary part
C_{11}	272.9 + 0.24 i	0.1	56.4
C_{22}	269.0 + 0.24 i	2.1	56.4
C_{12}	109.9 + 0.10 i	2.2	56.4
C_{66}	79.5 + 0.07 i	2.4	56.4

described. Finally, imaging results are given for several configurations, and a sensitivity study to apparatus parameters is performed.

2. The wave propagation model across the rail section and experimental validation

2.1. Mechanical characterization of the rail steel

Let us define x and y as the axis of the rail section and z as the axis along the rail length. The stiffness parameters of the steel composing the rail in the (x, y) plane are measured using an 18 mm-thick 60E1 rail sample. The sample is immersed in water, and 5-MHz ultrasonic pulses are transmitted through it with different incidence angles. The real parts of the stiffness parameters are obtained by measuring the times of flight [10], and the imaginary parts are obtained using frequency-domain transfer functions [11]. The values are presented in Table 1 with subscripts corresponding to the Voigt notation.

The stiffness parameters show that $C_{11} \cong C_{22}$ and $C_{11} \cong C_{12} + 2C_{66}$. Thus, the medium can reasonably be considered isotropic. The imaginary parts are very small, which implies that the damping effects are very small. This explains the poor measurement accuracy regarding the imaginary parts.

2.2. Propagation equations

The displacements corresponding to the x, y and z axes are written as u_x, u_y and u_z, respectively. The rail is assumed to be infinite in the z-direction, which implies that the along z-derivatives are zero in the orthotropic 3D-wave equation. This leads to two 2D-wave Eqs. Eq. (1) and Eq. (2). Eq. (1) corresponds to the propagation of both compressional and shear waves carrying a polarization in the (x, y) plane. This will subsequently be referred to as the in-plane polarization.

$$\rho\,\partial_t^2 \begin{pmatrix} u_x \\ u_y \end{pmatrix} - \begin{pmatrix} \partial_x & \partial_y \end{pmatrix} \times \begin{pmatrix} C_{11}\,\partial_x u_x + C_{12}\,\partial_y u_y & C_{66}\,(\partial_x u_y + \partial_y u_x) \\ C_{66}\,(\partial_x u_y + \partial_y u_x) & C_{12}\,\partial_x u_x + C_{22}\,\partial_y u_y \end{pmatrix} = \begin{pmatrix} 0 \\ 0 \end{pmatrix} \tag{1}$$

Eq. (2) corresponds to the propagation of shear waves with out-of-plane polarization, which is polarized along the z-direction.

$$\rho\,\partial_t^2 u_z - \begin{pmatrix} \partial_x & \partial_y \end{pmatrix} \begin{pmatrix} C_{55}\,\partial_x u_z \\ C_{44}\,\partial_y u_z \end{pmatrix} = 0 \tag{2}$$

It must be emphasized that the along-z non-dependency also applies to the sources. In practical applications with boundary transducers, this hypothesis is valid if the transducer dimension along the z-axis is large in comparison to the wavelength.

The equations are solved in the Laplace domain [12] using the PDE module of COMSOL Multiphysics software.[1] For the present application, this is equivalent to a frequency domain simulation using a frequency with a well-chosen imaginary part. This technique allows simulating wave propagation in media where the absence of PML or any absorption normally prevents frequency-domain simulation. This is an

[1] http://www.comsol.com

Fig. 2. The experimental apparatus for testing the numerical model.

alternative to time-domain truncated simulations. Using the COMSOL formalism [13], the implemented equations are written as follows:

$$\rho\omega^2\begin{pmatrix} u_x \\ u_y \end{pmatrix} + \nabla.\left(\begin{pmatrix} \begin{pmatrix} C_{11} & 0 \\ 0 & C_{66} \end{pmatrix} & \begin{pmatrix} 0 & C_{12} \\ C_{66} & 0 \end{pmatrix} \\ \begin{pmatrix} 0 & C_{66} \\ C_{12} & 0 \end{pmatrix} & \begin{pmatrix} C_{66} & 0 \\ 0 & C_{22} \end{pmatrix} \end{pmatrix}\nabla\begin{pmatrix} u_x \\ u_y \end{pmatrix}\right) = \begin{pmatrix} 0 \\ 0 \end{pmatrix} \tag{3}$$

$$\rho\omega^2 u_z + \nabla.\left(\begin{pmatrix} C_{55} & 0 \\ 0 & C_{44} \end{pmatrix}\right)\nabla u_z = 0 \tag{4}$$

$$\omega = 2\pi f - i\gamma \tag{5}$$

To obtain the corresponding time-truncated simulations, first an inverse Fourier transform and then an exponentially growing window $e^{\gamma t}$ are applied to the Laplace-domain simulations. The discretization step of the real part of the frequency is given as $1/T_{max}$, where T_{max} is the time-domain duration. The imaginary part of the frequency is constant. The real part of the frequency range of the simulation corresponds to that covered by the emission signal.

2.3. Geometry and boundary conditions

As said before, one requirement in the NDT of hundreds of kilometers of rails is easy access for one or several moving transducers. This reduces the possible location of an inspecting transducer array, for instance, to the upper side of the rail head. In Fig. 1(a), the thick blue line indicates the emission–reception boundary area. It is divided into eight parts corresponding to eight transducers. The simulated excitation signal is a 3-period sinusoidal burst. The Fourier transform coefficients of the signal are thus used as complex excitation magnitudes at each corresponding frequency in the numerical model. The excitation is a stress source oriented along the normal of the surface for in-plane polarization simulations. It is oriented along the z-axis for out-of-plane polarization simulations. The rail profile is the 60E1 profile, whose dimensions are given in Fig. 1(b).

2.4. Experimental validation of the defect-free propagation model

To assess the model validity, comparisons with pulse-echo experiments are performed on a real rail sample inspected using a single one-inch piezoelectric transducer with successively out-of-plane and in-plane polarizations. The transducer is located at the center of the upper side of the rail head, as presented in Fig. 2.

2.4.1. Out-of-plane polarization

Out-of-plane polarization waves are generated with a 1-MHz thick gel-coupled shear transducer. Shear waves propagate at approximately 3.2 mm/μs. The wavelength is thus approximately 3.2 mm at the central frequency, which is small in comparison to the transducer diameter (approximately one-eighth of the diameter). The z-axis independence assumption used for the numerical model is thus valid, and the radiation pattern in the rail section is expected to be narrow. The numerical and experimental measurements are compared in Fig. 3. The main echoes correspond to the successive reflections of the wave on the rail foot edge. The smaller signals in between correspond to multiple reflections in the rail head and web generated by the initial insonification or by the waves traveling back from the rail foot. The strong directivity of the device located at the center of the head surface tends to focus energy on the rail foot so that the contribution of the reflections back and forth from the foot is predominant in the measured signal. The back and forth propagation from head to foot lasts 107.8 μs in the simulated data and 106 μs in the experiments. The corresponding error is less than 2%. Such an agreement validates the real part of the C_{44} stiffness parameter. The decrease in the amplitudes of the successive echoes is similar in the simulation and experiments, meaning that the imaginary part of the C_{44} stiffness parameter is correct and that the z-component of the wavenumber is negligible.

2.4.2. In-plane polarization

In-plane polarization waves are generated with a 1-MHz gel-coupled longitudinal transducer. At this frequency, longitudinal waves have a 6-mm wavelength corresponding to approximately a quarter of the transducer diameter. Thus, the radiation pattern of the transducer is expected to be larger than that for the out-of-plane experiment. The corresponding signals are presented in Fig. 4.

In contrast to the out-of-plane measurements, the contribution of the multiple reflections in the rail head and that coming from the rail foot are similar. This is due to the larger aperture of the device, which produces more waves trapped in the rail head. This explains the complex response of the structure where wave packets can hardly be distinguished. The large echoes arising after 16 μs in the experiments and the simulations correspond to the reflection without polarization conversion at the bottom of the rail head and are simultaneous. The echoes arising after 58 μs and 58.2 μs correspond to the reflection without polarization conversion on the rail foot, respectively. The corresponding error on the wave velocity is 0.3% and thus validates the real part of C_{11}.

The angular aperture is also large in the (y, z) plane. Thus, the along-z infinite transducer hypothesis is not fully satisfied. As mentioned earlier, the wavelength is not that small compared to the transducer size, which means that propagation along the z-axis cannot be fully neglected. This along-z propagation logically causes extra attenuation of the signals within the section that is not taken into account in the model. This leads to a quicker decay of the experimental signal than in the simulated signal.

3. The imaging procedure

3.1. The defects under investigation

Many different defects may alter the rail integrity. In the present work, three specific defects are investigated (Fig. 5). Vertical cracks

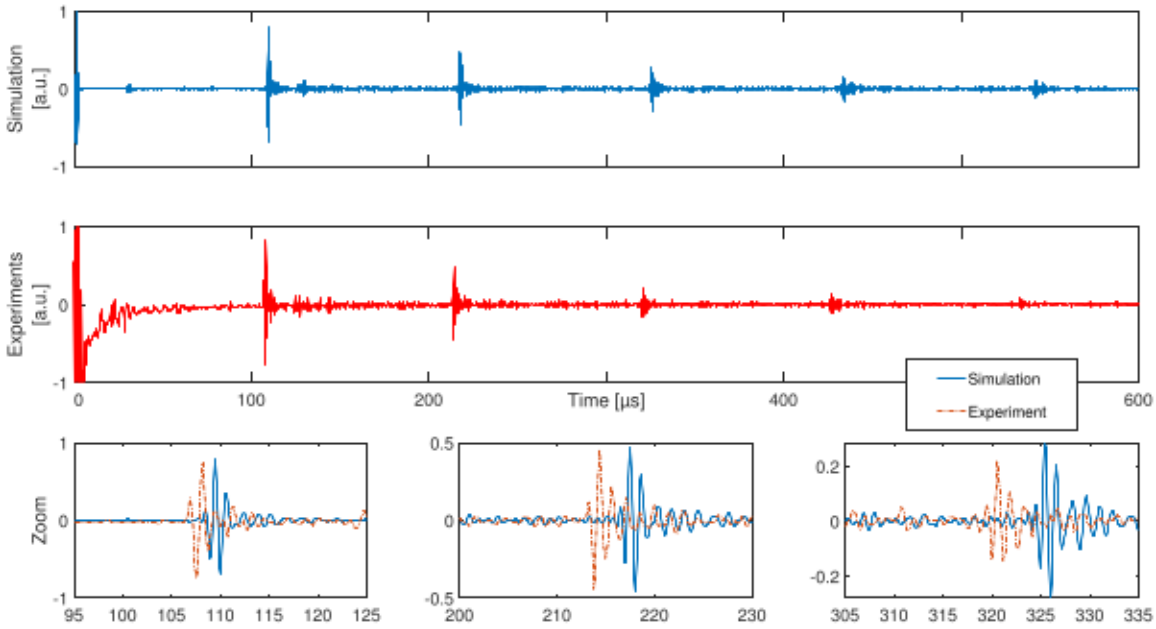

Fig. 3. Out-of-plane polarization with a 1-MHz central frequency.

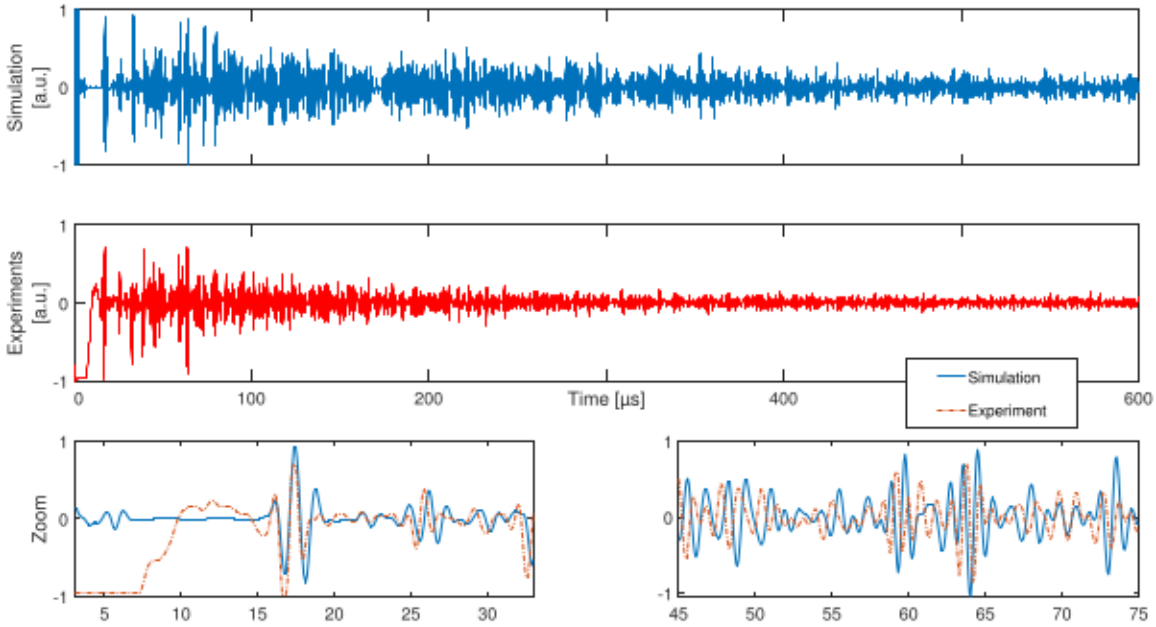

Fig. 4. In-plane polarization with a 1-MHz central frequency.

(Fig. 5a) are simulated in the numerical model as a 30-μm thin elongated crack presenting two close reflecting interfaces. The crack height is 5 mm, and the total interface length is 10 mm. Corrosion may result in a loss in material under the foot. A corrosion pit (Fig. 5b) is simulated as a half oval shape missing material. The horizontal length and the height of the pit are 20 mm and 5 mm, respectively. Rail injury (Fig. 5c) is another material loss usually appearing at the lateral tips of the rail foot. One is simulated here as a 5 mm radius missing circle.

3.2. Generation of the synthetic measurements

The synthetic measurements are generated using the model described in Section 2. The medium is assumed to be isotropic, which is reasonable regarding the stiffness parameters. The shortest path from the top of the head to the lateral tip of the rail foot is approximately 250 mm. Knowing that the wave paths are not direct, the authors choose to consider 500 mm as a reasonable maximal wave distance between the transducers and the possible defect. The corresponding back and forth distance is close to 1000 mm. The slowest wave velocity is 3.2 mm/μs, and the corresponding propagation duration is approximately 300 μs. This duration is chosen as the typical truncation time applied to the synthetic measurements. Nevertheless, the sensitivity to this parameter is studied in Section 4.

The central frequency is chosen so that the corresponding wavelength is on the order of magnitude of the defects, i.e., approximately 10 mm. A value of 0.5 MHz is chosen as the typical central frequency, as it corresponds to wavelengths of 6.4 mm and 11.8 mm for transverse and longitudinal waves, respectively. Nevertheless, the sensitivity to the central frequency is studied in Section 4. The time-domain excitation signal is a classical 3-period windowed sinusoidal signal with

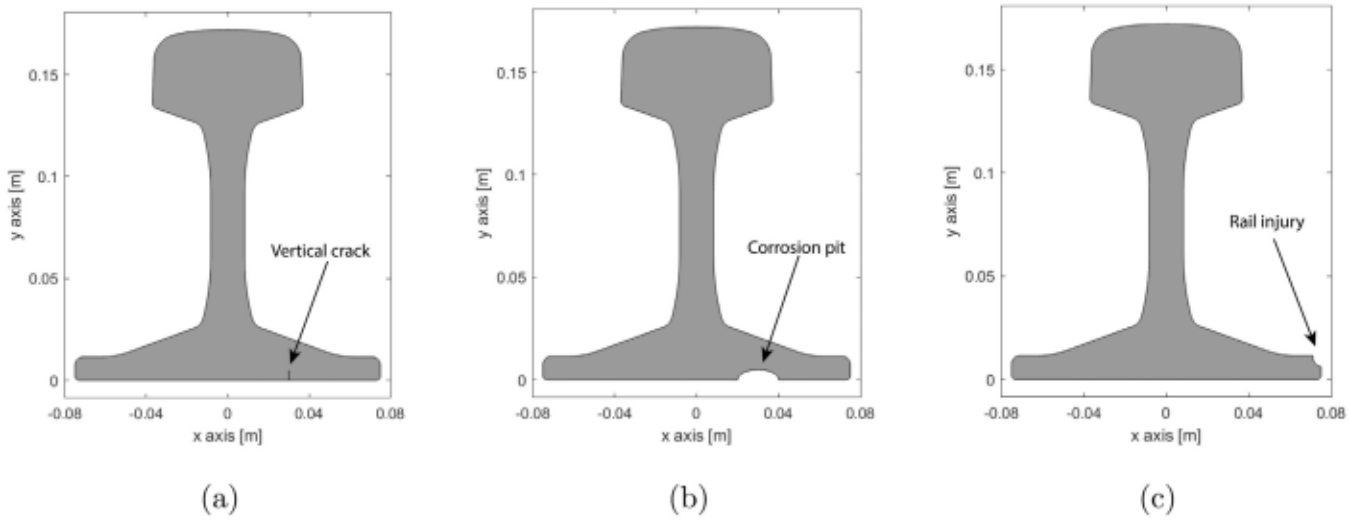

Fig. 5. The different defects under investigation: (a) longitudinal vertical crack, (b) corrosion pit, and (c) rail injury.

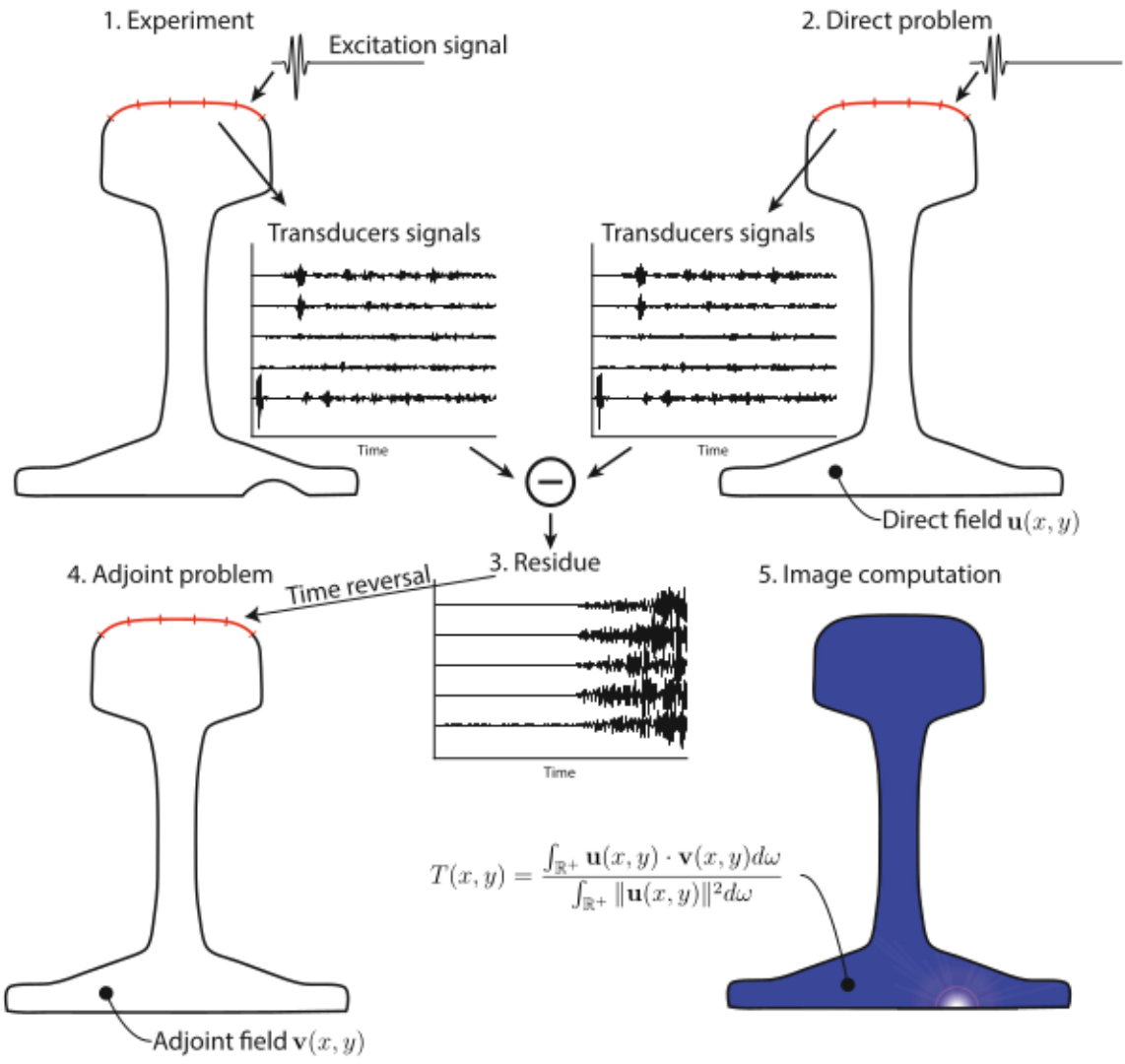

Fig. 6. Application of the topological imaging framework to 2D rail investigation.

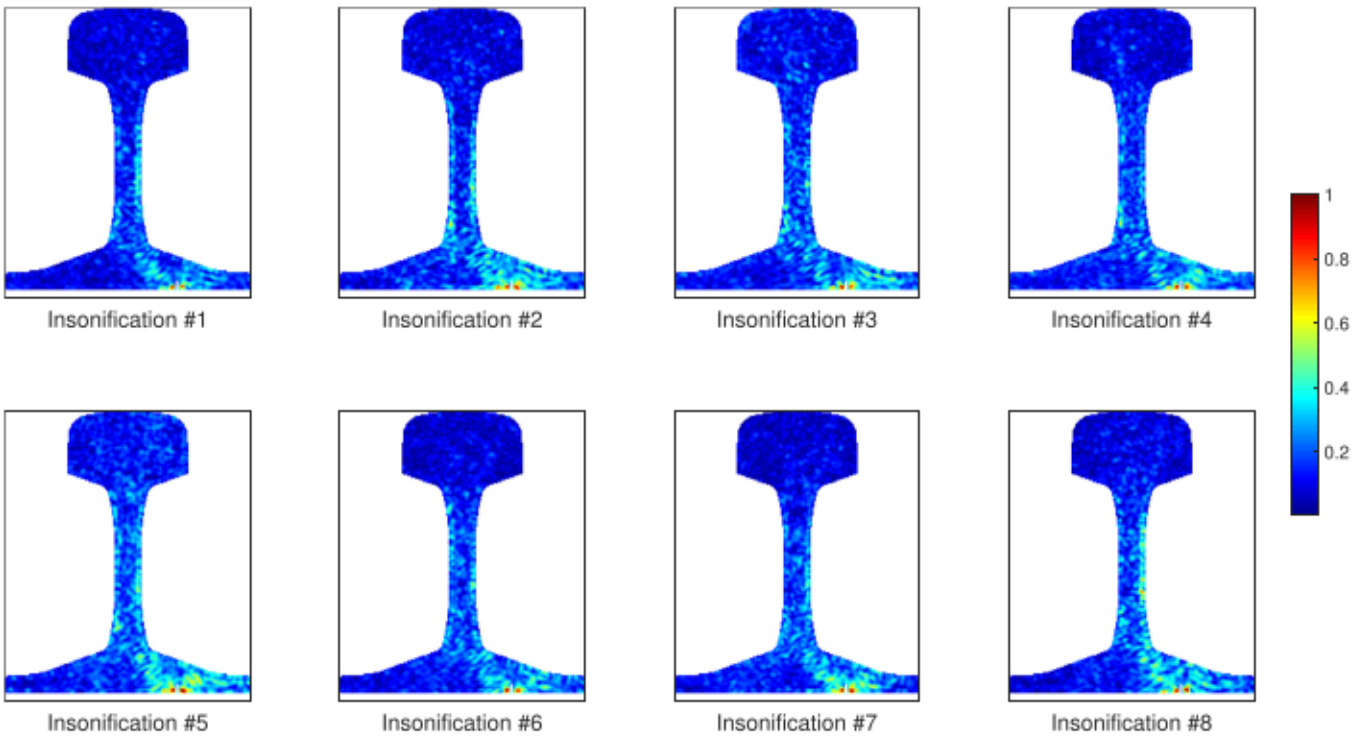

Fig. 7. Topological images of the rail section presenting a longitudinal vertical crack. The defect is represented by a white line. Eight transducers are simulated, and each image is successively obtained using one of the transducers as the emitter. The polarization is in the rail plane. The acquisition time is 300 μs. Each image is normalized between 0 and 1.

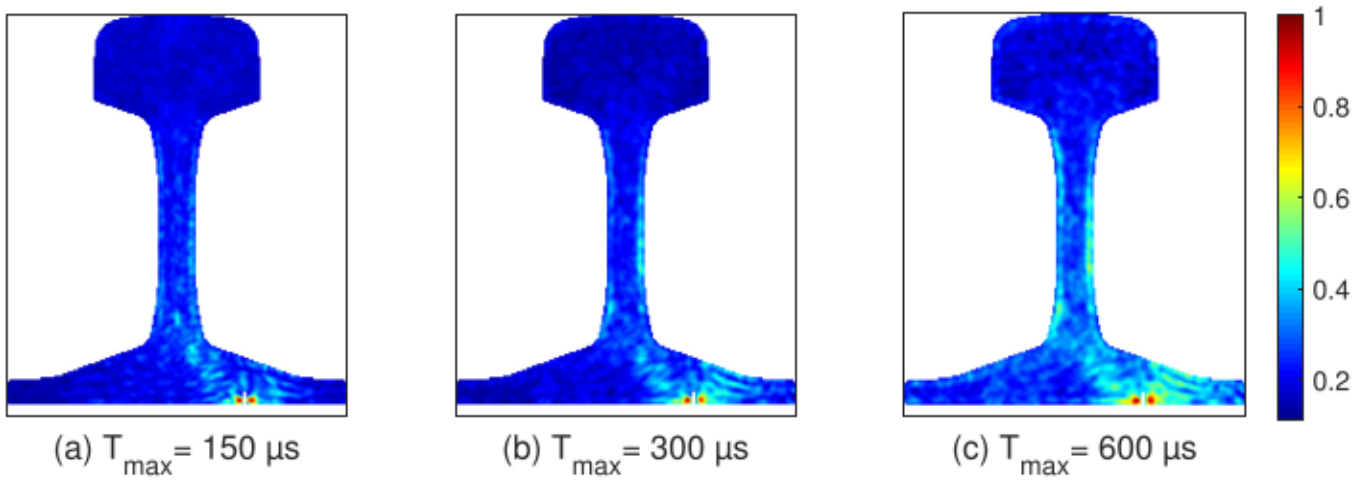

Fig. 8. Topological images of the rail section presenting a longitudinal vertical crack. The defect is represented by a white line. Each image is computed considering acquisition durations of 150, 300 and 600 μ. The polarization is in the rail plane, and 16 transducers are used.

a unity magnitude. The corresponding Fourier-transformed coefficients are used as stress boundary sources in the frequency-domain model.

Classical transducer arrays typically have a pitch equal to half the wavelength at the central frequency. Knowing that the chosen transducer area is approximately 80 mm long, a 16-transducer array should be adequate. One of the advantages of using reverberated acoustic information is the small number of transducers required. For instance, in [9], almost half wavelength resolution is achieved by taking advantage of the reverberating nature of the structure using a single transducer. However, truncating the time domain implies that only a part of the reverberated information is taken into account. It will be shown in the last section that the number of transducers can be reduced without significant quality loss. It must be noted that the same time domain is used for all measurements and all transducers.

3.3. Application of the topological imaging framework to the rail section

The image construction can be summarized in the five steps presented in Fig. 6:

1. The first step is the generation of the synthetic measurements. In the figure example, 5 transducers are drawn for clarity, and the fifth is used as the source (excitation signal). The defect is located on the right side of the rail foot. The five measurement signals are shown in the transducer signal box.
2. The second step corresponds to the direct problem computation. The same source as in step 1 is used, but the rail is free of defects. The outputs of the second step are the transducer signals used in step 3 and the global radiated wavefield $\mathbf{u}(x, y, \omega)$ used in step 5. If in-plane polarization is considered (Eq. (1)), $\mathbf{u}(x, y, \omega)$ =

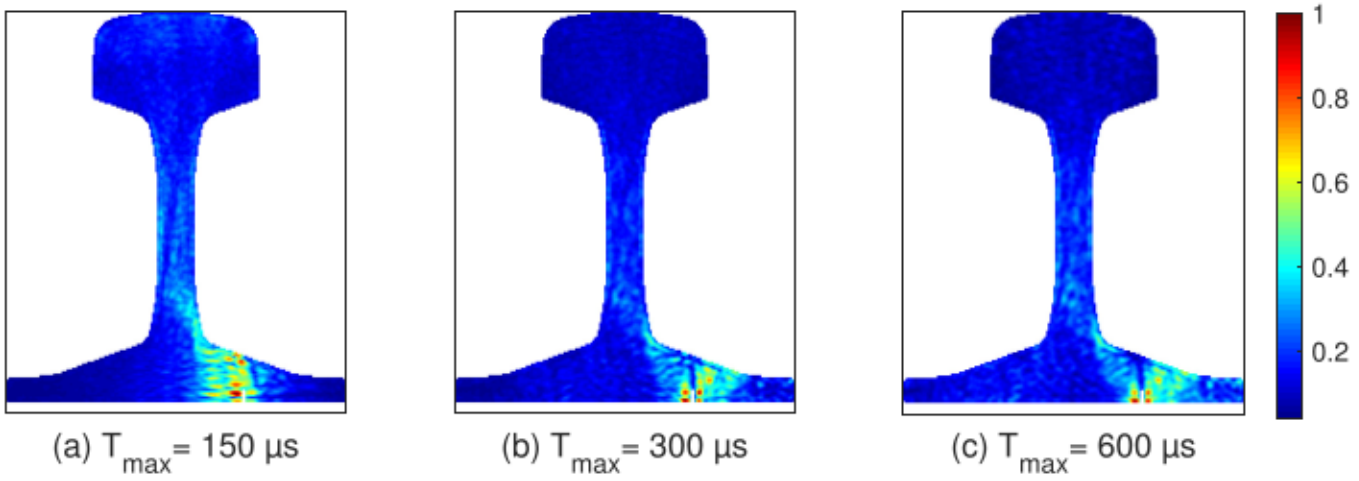

Fig. 9. Topological images of the rail section presenting a longitudinal vertical crack. The defect is represented by a white line. The polarization is out of the rail plane. Each image is computed considering acquisition durations of 150, 300 and 600 µs, and 16 transducers are used.

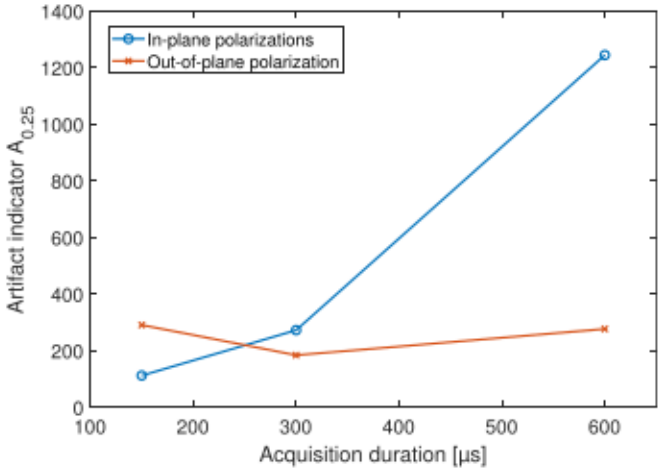

Fig. 10. Influence of the acquisition duration on the artifact indicators for images computed with a central frequency of 500 kHz, $N = 16$ transducers and in the presence of a vertical crack.

$u_x\,\mathbf{e_x} + u_y\,\mathbf{e_y}$. If out-of-plane polarization is considered (Eq. (2)), $\mathbf{u}(x, y, \omega) = u_z\,\mathbf{e_z}$.

3. The third step is residue computation, defined as the difference between the transducer signals obtained in step 1 (in the presence of defects) and those obtained in step 2 (in the absence of defects). The residue corresponds to the acoustic signature of the defect. This explains the zero values within the acquisition time domain corresponding to the first back and forth propagation between the transducer array and the defect.
4. Step 4 is the adjoint problem computation. The source is the time-reversed residue, and the rail is free of defects. In the frequency domain, the source is the conjugated residue. The wavefield obtained is denoted $\mathbf{v}(x, y, \omega)$. Similar to step 2, if in-plane polarization is considered, $\mathbf{v}(x, y, \omega) = v_x\,\mathbf{e_x} + v_y\,\mathbf{e_y}$. If out-of-plane polarization is considered, $\mathbf{v}(x, y, \omega) = v_z\,\mathbf{e_z}$.
5. The last step is the image computation obtained from both direct and adjoint wavefields, respectively $\mathbf{u}(x, y, \omega)$ and $\mathbf{v}(x, y, \omega)$. The function $T(x, y)$ corresponds to a normalized topological gradient [9,14]. It is given by:

$$T(x,y) = \frac{\left|\int_{\mathbb{R}^+} \mathbf{u}(x,y,\omega)\mathbf{v}(x,y,\omega)d\omega\right|}{\int_{\mathbb{R}^+} \|\mathbf{u}(x,y,\omega)\|^2 d\omega} \tag{6}$$

The numerator is a topological gradient, whereas the denominator corresponds to the insonification intensity. The denominator allows compensation for the over-insonification of the rail head and the poor insonification of the foot due to the rail geometry. The imaging function $I(x, y)$ used in this paper corresponds to the normalization between 0 and 1 of $T(x, y)$. Thus, it is defined as:

$$I(x,y) = \frac{T(x,y)}{\max(T(x,y))} \tag{7}$$

Subsequently, the array is composed of N transducers for both in-plane and out-of-plane polarizations. Each transducer is successively used as the emitter, and thus, N different sets of measurements are obtained. Each set is composed of N signals, one for each receiver. This procedure is also referred to as the full matrix capture [15]. Each set is used to compute an image following the methodology described in Fig. 6. The final image is the mean value of the N obtained images.

4. Imaging results

Despite the fact that specific attention is given to the rail foot in the present work, defects in any part of the rail can be detected with the present method. That is why the whole rail section is drawn so that possible imaging artifacts can be discussed.

4.1. The artifact indicator

To compare the magnitude of artifacts, a quantitative function A_m, called the artifact indicator, is defined as follows:

$$A_m = \int I(x,y)\,\delta_{I(x,y)>m}\,\delta_{d_{\text{defect}}(x,y)>6\text{ mm}}\,dS \tag{8}$$

where δ stands for the Kronecker symbol and $d_{\text{defect}}(x, y)$ is the distance of point (x, y) to the nearest defect boundary. A_m corresponds to the surface of the image exceeding the value m out of the defect vicinity weighted by the image intensity at the corresponding locations. The vicinity of the defect is taken as 6 mm. The artifact indicator quantifies the overall artifact intensity in mm^2. It can be compared to the total surface of the rail section, i.e., 7671 mm^2. It must be noted that this indicator does not take into account the location of the artifact or whether it is widespread or concentrated. In all the results presented in this paper, the value 1 is reached in the defect vicinity. Nevertheless, high values in another location would indicate a secondary defect that is not present. $A_{0.5}$ is thus a good indicator for possible false positive diagnoses. $A_{0.25}$ will be used to compare image quality.

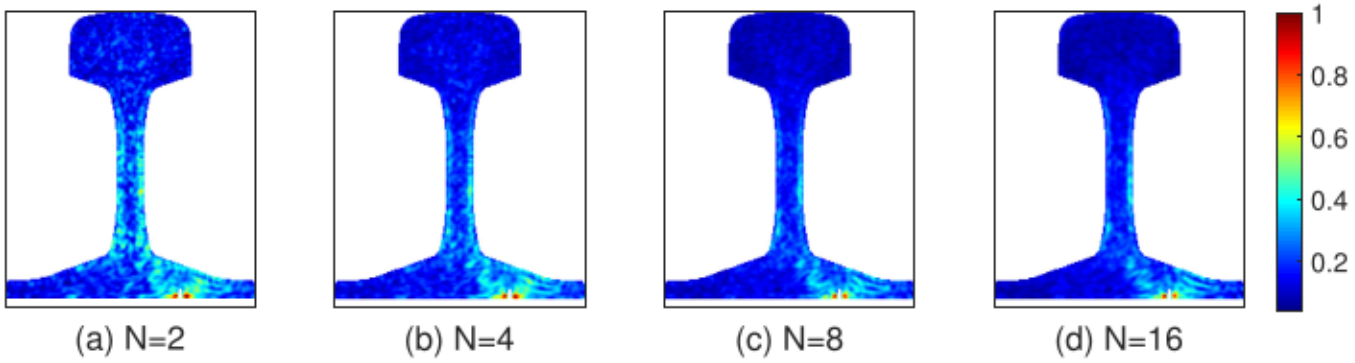

Fig. 11. Topological images of the rail section presenting a longitudinal vertical crack. The defect is represented by a white line. Each image is computed considering 2, 4, 8 and 16 transducers. The polarization is in the rail plane. The acquisition duration is 300 μs.

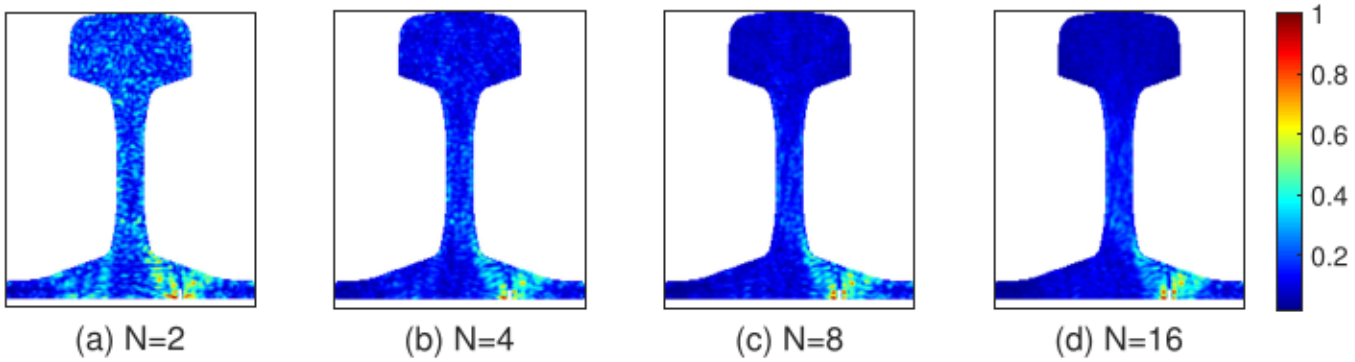

Fig. 12. Topological images of the rail section presenting a longitudinal vertical crack. The defect is represented by a white line. Each image is computed considering 2, 4, 8 and 16 transducers. The polarization is out of the rail plane. The acquisition duration is 300 μs.

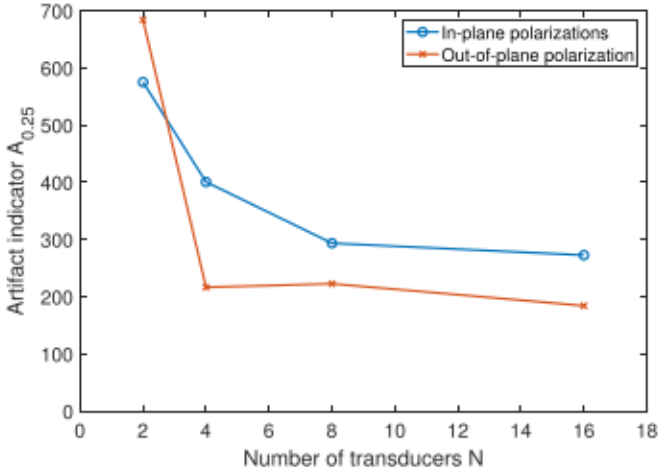

Fig. 13. Influence of the number of transducers on the artifact indicators for images computed with a central frequency of 500 kHz and in the presence of a vertical crack.

4.2. Influence of averaging

The final images are defined as the mean value of several images. In the example of Fig. 7, $N = 8$ transducers are used to cover the transducer surface, and 8 different insonifications are performed, each leading to a set of measurements and to one image. In the present example, each insonification is performed using a single transducer as the emitter. Nevertheless, any kind of insonification with any transducers is also eligible in the method. First, it must be emphasized that the signature of the defect is to be seen on each image and that it corresponds to the highest values of each image, i.e., a unity magnitude. Nevertheless, widespread artifacts have a significant magnitude. Taking the mean value of these images leads to the image in Fig. 11(c). The mean values of the artifact indicators $A_{0.5}$ and $A_{0.25}$ of the 8 images are 14.2 mm^2 and 313.8 mm^2, respectively, versus 2.8 mm^2 and 255.7 mm^2 for the mean-valued image. This means that most artifacts are below 0.5. Those above 0.5 are efficiently reduced by computing the image mean value. The predominant artifacts are between 0.25 and 0.5. Depending on the insonification, some one-insonification images present a smaller $A_{0.25}$ than the mean image; however, it is not possible to know which insonification is the best without the defect knowledge. Nevertheless, the artifact indicator $A_{0.25}$ of the mean image is smaller than the mean indicator of the 8 images.

The influence of the different transducer array parameters is first studied to design the setup. For these studies, the vertical crack is taken as the defect.

4.3. Influence of the acquisition duration

The acquisition duration defines the amount of reverberated field taken into account. When taking a duration that is too short, no information has the time to travel from the array to the defect and back to the array. When taking a short duration, only the first interactions among the incoming field, the surrounding medium and the defect are measured. When taking a longer duration, complex multiple interactions are also measured. The sensitivity of the image to the acquisition duration is studied in Fig. 8 and Fig. 9 for in-plane and out-of-plane polarizations, respectively, and in Fig. 10.

One could expect an improvement with increasing duration as more physical information is taken into account. For instance, for out-of-plane polarization, the artifact magnitude decreases when increasing the acquisition duration from 150 μs to 300 μs. However, this is not the case for in-plane polarization, as there are clearly more artifacts

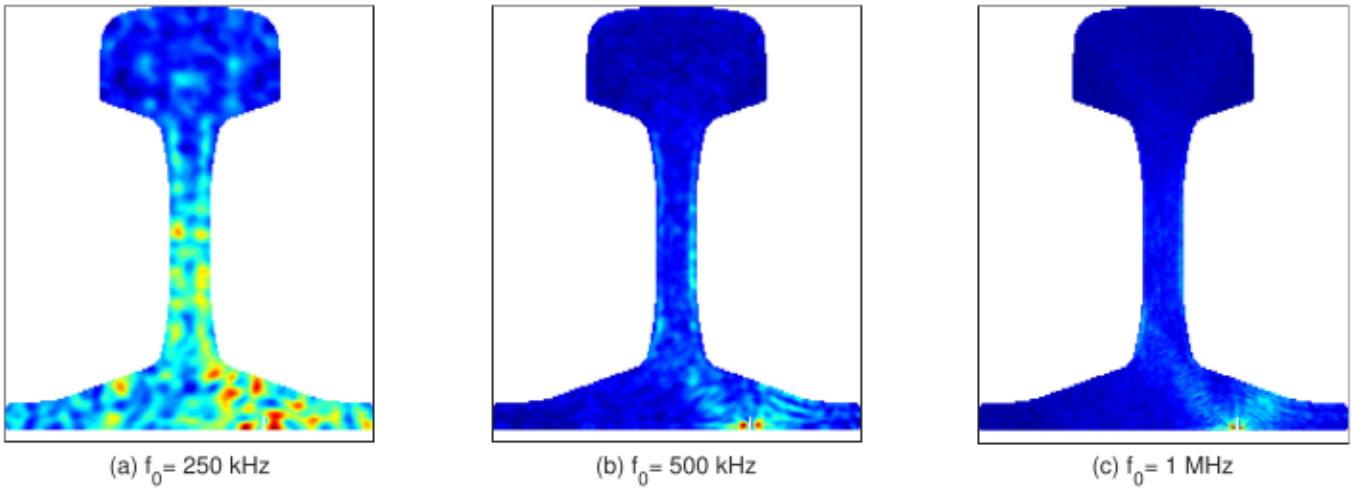

Fig. 14. Topological images of the rail section presenting a longitudinal vertical crack. The defect is represented by a white line. Each image is computed considering central frequencies of 250, 500 and 1000 kHz. The polarization is in the rail plane. The acquisition duration is 300 μs, and the number of transducers is 16.

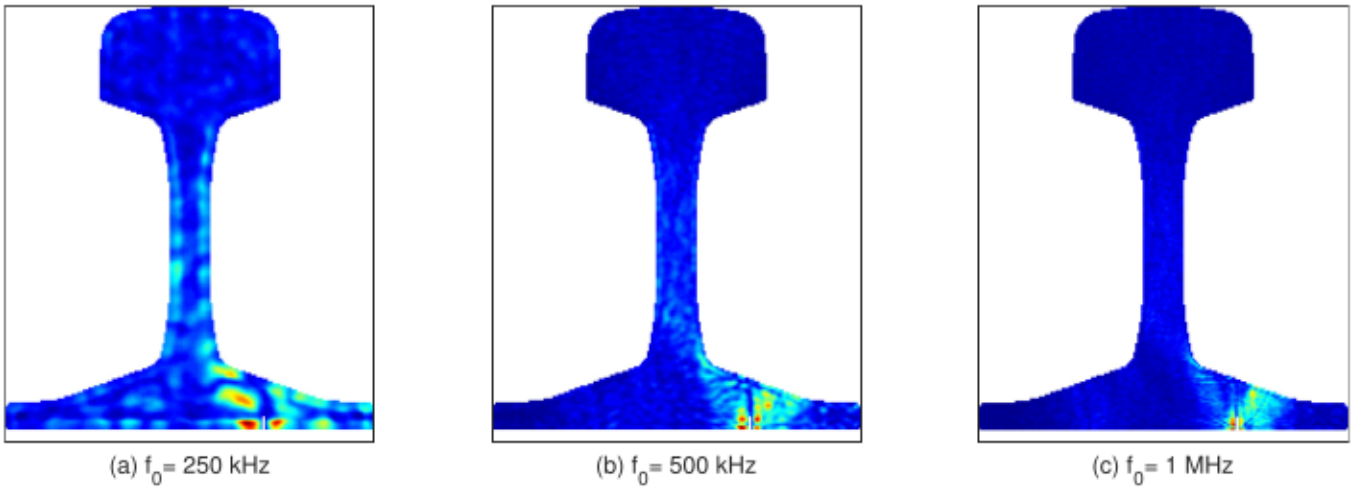

Fig. 15. Topological images of the rail section presenting a longitudinal vertical crack. The defect is represented by a white line. Each image is computed considering central frequencies of 250, 500 and 1000 kHz. The polarization is normal to the rail plane. The acquisition duration is 300 μs, and the number of transducers is 16.

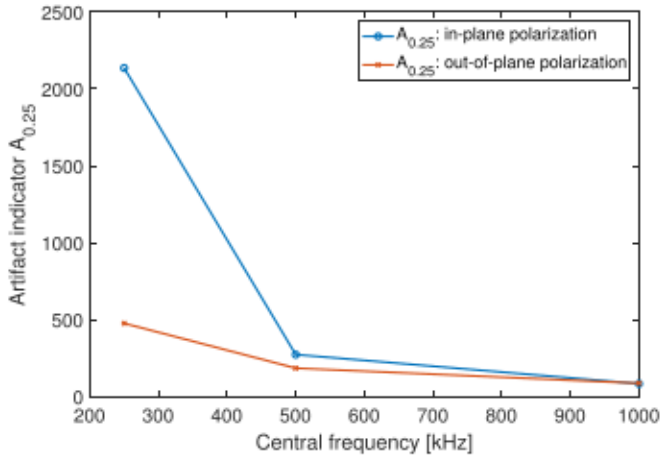

Fig. 16. Influence of the central frequency on the artifact indicators for images computed in the presence of a vertical crack.

when increasing the acquisition duration from 300 μs to 600 μs. To summarize these results, the artifact indicators of these images are plotted in Fig. 10.

To understand these results, it must be reminded that the experimental information carrying the defect signature is used in a defect-free medium through direct and adjoint problems. Thus, only the first-order interaction between the defect and the surrounding medium can be properly taken into account in the imaging principle. This corresponds to the so-called Born approximation. This approximation is valid for small or low-contrast defects. Here, the defects have a high contrast and are large, as their size is typically of the wavelength order. That is why long-lasting measurements do not necessarily lead to better results, as they carry the signature of multiple interactions between the defect and the surrounding medium. In-plane polarization waves are either longitudinal or transverse, whereas out-of-plane polarization waves are only transverse. As the velocity of longitudinal waves is nearly twice as large, the discussed issue with long-lasting signals arises with shorter acquisition duration.

4.4. Influence of the number of transducers

The number of transducers covering the transducer area would typically be 16 for a classical method that assumes a semi-infinite

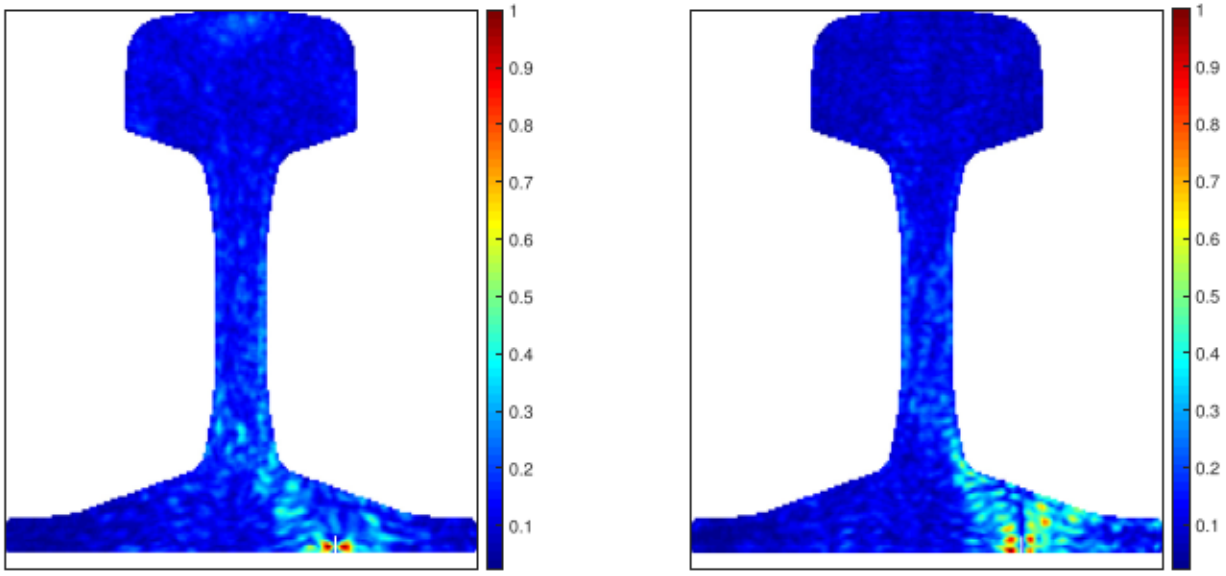

Fig. 17. Topological images of the rail section presenting a longitudinal vertical crack. The defect is represented by a white line.

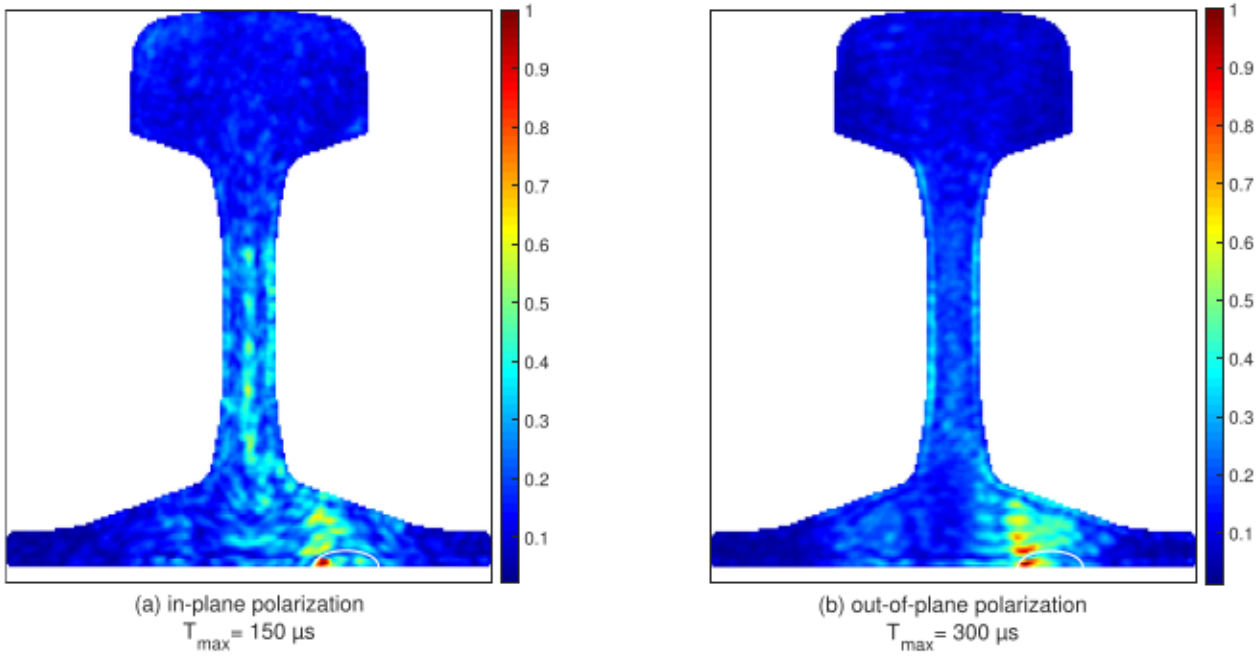

Fig. 18. Topological images of the rail section presenting a corrosion pit. The defect boundary is represented by a white line.

medium to compute the image following the half wavelength principle. Here, taking advantage of a part of the reverberated field, one can expect good results with fewer transducers. Its influence is presented in Fig. 11 and Fig. 12 for in-plane and out-of-plane polarizations, respectively.

In both cases, a significant improvement is obtained when increasing the number of transducers from 2 to 4, and a smaller improvement seems to be obtained when increasing the number from 4 to 8. These observations are quantified by computing the artifact indicators presented in Fig. 13. The described improvements are intuitive, as increasing the number of transducers gives both richer experimental information and a higher number of different insonifications. However, the improvement when increasing from 8 to 16 transducers is not significant. In both cases, 8 transducers seem to be enough for a 500 kHz central frequency.

4.5. Influence of the central frequency

The influence of the central frequency of the wave packet is studied in Fig. 14 and in Fig. 15. The improvement of the images when increasing the central frequency from 250 to 500 kHz is spectacular, especially for the in-plane polarization case. A further improvement is obtained when increasing the central frequency up to 1 MHz. The sensitivity of the artifact indicator to the central frequency is plotted in Fig. 16. Increasing the central frequency clearly reduces artifacts, especially those in the web. We propose two leads to explain this

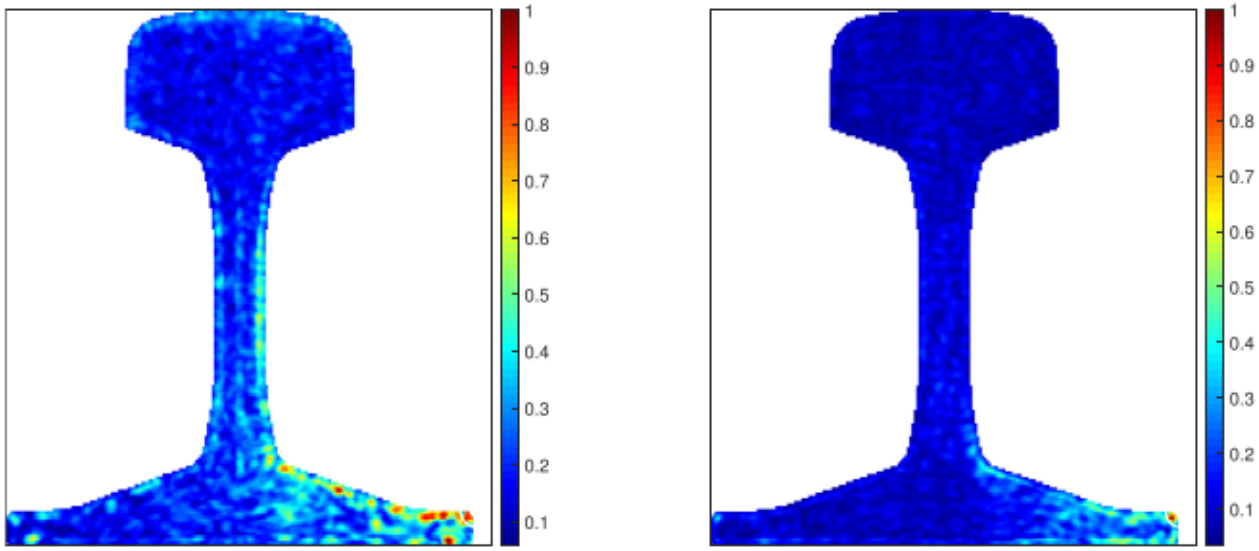

Fig. 19. Topological images of the rail section presenting a rail injury. The defect boundary is represented by a white line.

phenomenon. The first argument is the higher resolution obtained when using a smaller wavelength, as it is also stated in unbounded media. The second argument is linked to the possible overlapping of the frequency range with vibrating modes of the structures when choosing a low central frequency. In fact, activating a resonance in a structure tends to strongly alter the image as one frequency component becomes predominant. A predominant frequency component has a similar effect as using a long-lasting pulse, i.e., a short frequency range pulse. It strongly reduces resolution in an unbounded medium and thus may lead to strong artifacts in a bounded medium.

It should be noted that simulating a 3-period excitation centered at 1 MHz leads to 565 frequency steps for frequencies up to 1.86 MHz for each field computation. The images presented in Figs. 14(c) and 15(c) are defined as the mean values of 16 images, each one requiring 3 field computations. Under these conditions, it took approximately 16 days to obtain these final images using a 4-core 8-thread 3.7 GHz CPU.

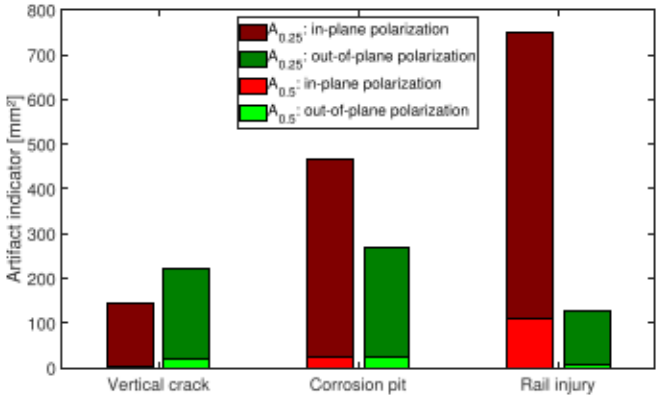

Fig. 20. Comparison of the artifact indicators of the images of the three defects under investigation.

4.6. Images obtained for the typical defects under study

Following the observations made in the sensitivity study, acquisition durations of 150 µs and 300 µs are chosen for in-plane and out-of-plane polarizations, respectively. $N = 8$ transducers are used with a central frequency of 500 kHz. Choosing a central frequency of 500 kHz instead of 1 MHz despite more promising results at 1 MHz is motivated by seeking robustness. Even if the sensitivity to unpredicted geometrical variations is out of the scope of this work, one should expect that the smaller the wavelength is, the more sensitive to geometrical variations. We thus chose the smallest central frequency allowing acceptable results. In the present context, it is 500 kHz.

The topological images corresponding to the defect presented in Fig. 5(a) and obtained with 8 transducers and a central frequency of 500 kHz are presented in Fig. 17. For each polarization type, the vertical crack is detected and accurately located. Imaging artifacts can also be observed. In this example, artifacts are of slightly smaller magnitude for the in-plane polarization.

The topological images corresponding to the defect presented in Fig. 5(b) obtained with eight transducers are presented in Fig. 18. For both polarization types, the corrosion pit is detected, and only the left-hand side edge (close to the $x = 0$ axis) is located. Imaging artifacts are also visible. In this example, artifacts are of a larger magnitude and more widespread for the in-plane polarization than for the out-of-plane polarization.

The topological images corresponding to the defect presented in Fig. 5(c) obtained with eight transducers are presented in Fig. 19. For both polarizations, the injury is detected. It is more clearly located with the out-of-plane polarization due to the artifacts, which are of smaller magnitude and less widespread in this case.

The artifact indicators $A_{0.25}$ and $A_{0.5}$ are compared for each investigated defect in Fig. 20. For the studied array configurations, the out-of-plane polarization produces fewer artifacts globally. The high $A_{0.5}$ indicator of the corrosion pit and the injury cases for the in-plane polarization indicates a higher risk of detecting absent secondary defects leading to false positive diagnoses at some locations.

4.7. Sensitivity to inaccurate material properties

The previous results are obtained in the ideal situation where the material properties are accurately known. When inspecting a medium that is globally unbounded, a velocity error mainly results in a space-distorted image. The defects are simply localized too far of too near from the array. When inspecting a masked area of a bounded medium, it is expected that such an error induces worse consequences. In order

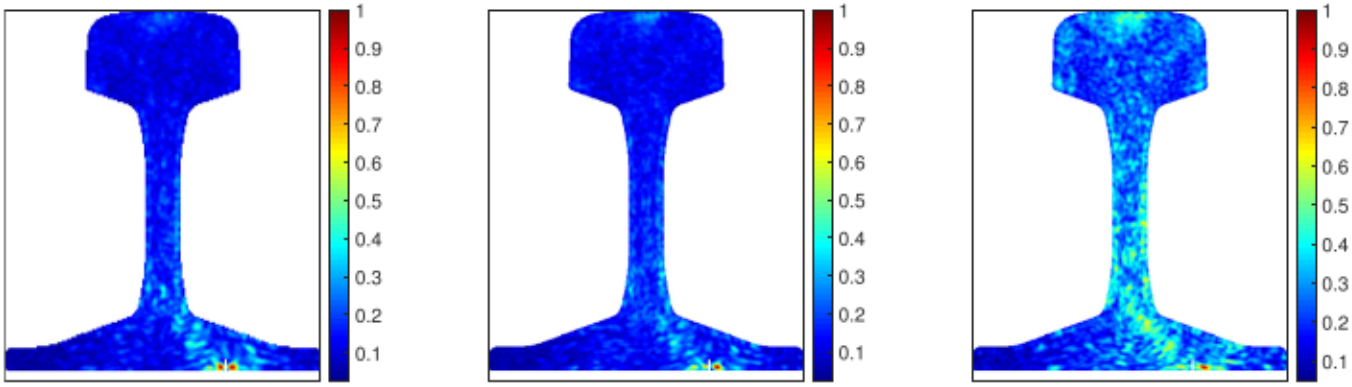

Fig. 21. Effect of an increasingly inaccurate velocity for building the images. The vertical crack case under in-plane wave investigation.

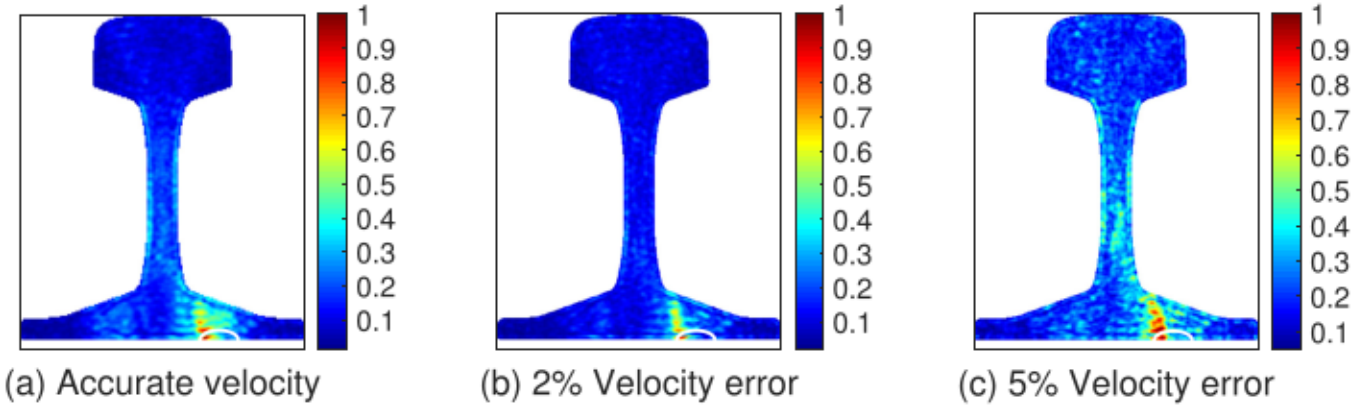

Fig. 22. Effect of an increasingly inaccurate velocity for building the images. The corrosion pit case under out-of-plane wave investigation.

to sense the effect of property inaccuracy, the vertical crack and the corrosion pit cases are rerun assuming inaccurate wave velocity when computing wavefields $\mathbf{u}(x, y, \omega)$ and $\mathbf{v}(x, y, \omega)$ used to compute the image (Eqs. ((6),(7))). The velocity values are successively increased by 2 and 5 percent. The corresponding images are given respectively in subfigures (b) and (c) of Figs. 21 and 22. Keeping the inaccuracy below 2 percent makes it possible to maintain the image quality. Increasing it up to 5 percent strongly increases artifact magnitude despite a still correct defect localization. We expect that higher inaccuracy leads to imaging procedure failure. This relatively high sensitivity to the material properties implies that a careful experimental characterization is necessary for practical implementation of the method.

5. Conclusion

In this paper, truncated-time topological imaging potentiality is successfully assessed for detecting defects in the rail foot using transducers located on the rail head. Simulated longitudinal vertical cracks, corrosion pits and rail injuries are successfully detected. The locations of the crack and the injury are accurate, but only a part of the corrosion pit boundary is located. The imaging artifacts tend to be of smaller magnitude when inspected with out-of-plane polarization. The next step is to perform real experiments with real defects and to assess the robustness of the method versus possible unpredictable changes in the geometry of railways. The experimental setup will require the development of a specific transducer array that combines a relatively low central frequency (typically 0.5 to 1 MHz) and a relatively low transducer number (typically 8 or 16) and adapts to the shape of the rail head. A contact-less solution would be ideal. EMATs (electromagnetic acoustic transducers) could be candidates, but shaping EMAT array is still at the research stage. Otherwise, a wedge could be used with a more conventional still nonstandard PZT array. The latter solution only enables in-plane polarization solutions. The specific development of an experimental device and its corresponding numerical simulation will be the subject of a new study.

CRediT authorship contribution statement

Samuel Rodriguez: Conceptualization, Investigation, Software, Writing – original draft. **Victor Gayoux:** Software, Investigation. **Eric Ducasse:** Software, Investigation. **Michel Castaings:** Resources, Investigation. **Nicolas Patteeuw:** Resources, Supervision.

Declaration of competing interest

The authors declare that they have no known competing financial interests or personal relationships that could have appeared to influence the work reported in this paper.

Acknowledgments

This study was supported by the National society of French railroads SNCF.

References

[1] Innotrack consortium. D4.4.1 – Rail inspection technologies. Tech. rep., 2008, URL https://www.charmec.chalmers.se/innotrack/deliverables/sp4/d441-f3p-rail_inspection_technologies.pdf.

[2] Fan Y, Dixon S, Edwards RS, Jian X. Ultrasonic surface wave propagation and interaction with surface defects on rail track head. NDT & E Int 2007;40(6):471–7. http://dx.doi.org/10.1016/j.ndteint.2007.01.008.

[3] Kim G, Seo MK, Kim YI, Kwon S, Kim KB. Development of phased array ultrasonic system for detecting rail cracks. Sensors Actuators A 2020;311:112086. http://dx.doi.org/10.1016/j.sna.2020.112086.

[4] Zumpano G, Meo M. A new damage detection technique based on wave propagation for rails. Int J Solids Struct 2006;43(5):1023–46. http://dx.doi.org/10.1016/j.ijsolstr.2005.05.006.

[5] Hu S, Shi W, Lu C, Chen Y, Chen G, Shen G. Rapid detection of cracks in the rail foot by ultrasonic B-scan imaging using a shear horizontal guided wave electromagnetic acoustic transducer. NDT & E Int 2021;120(2020):102437. http://dx.doi.org/10.1016/j.ndteint.2021.102437.

[6] Pathak M, Alahakoon S, Spiryagin M, Cole C. Rail foot flaw detection based on a laser induced ultrasonic guided wave method. Measurement: J Int Measur Confederation 2019;148:106922. http://dx.doi.org/10.1016/j.measurement.2019.106922.

[7] Bonnet M, Guzina BB. Sounding of finite solid bodies by way of topological derivative. Internat J Numer Methods Engrg 2004;61(2003):2344–73. http://dx.doi.org/10.1002/nme.1153.

[8] Dominguez N, Gibiat V, Esquerre Y. Time domain topological gradient and time reversal analogy: an inverse method for ultrasonic target detection. Wave Motion 2005;42(1):31–52. http://dx.doi.org/10.1016/j.wavemoti.2004.09.005.

[9] Rodriguez S, Veidt M, Castaings M, Ducasse E, Deschamps M. One channel defect imaging in a reverberating medium. Appl Phys Lett 2014;105(24):244107. http://dx.doi.org/10.1063/1.4904837.

[10] Hosten B, Deschamps M. Inhomogeneous wave generation and propagation in lossy anisotropic solids. Application to the characterization of viscoelastic composite materials. J Acoust Soc Am 1987;82:1763–70. http://dx.doi.org/10.1121/1.395170.

[11] Castaings M, Hosten B, Kundu T. Inversion of ultrasonic, plane-wave transmission data in composite plates to infer viscoelastic material properties. NDT & E Int 2000;33(6):377–92. http://dx.doi.org/10.1016/S0963-8695(00)00004-9.

[12] Mora P, Ducasse E, Deschamps M. Transient 3D elastodynamic field in an embedded multilayered anisotropic plate. Ultrasonics 2016;69:106–15. http://dx.doi.org/10.1016/j.ultras.2016.03.020.

[13] COMSOL. [COMSOL multiphysics®] v. 5.4 Reference Manual. 2018, URL www.comsol.com.

[14] Rodriguez S, Deschamps M, Castaings M, Ducasse E. Guided wave topological imaging of isotropic plates. Ultrasonics 2014;54(7):1880–90. http://dx.doi.org/10.1016/j.ultras.2013.10.001.

[15] Holmes C, Drinkwater BW, Wilcox PD. Post-processing of the full matrix of ultrasonic transmit-receive array data for non-destructive evaluation. NDT & E Int 2005;38:701–11. http://dx.doi.org/10.1016/j.ndteint.2005.04.002.